Volume 14
Number 8
August 2021
Pages 4135–4622

Energy & Environmental Science

rsc.li/ees

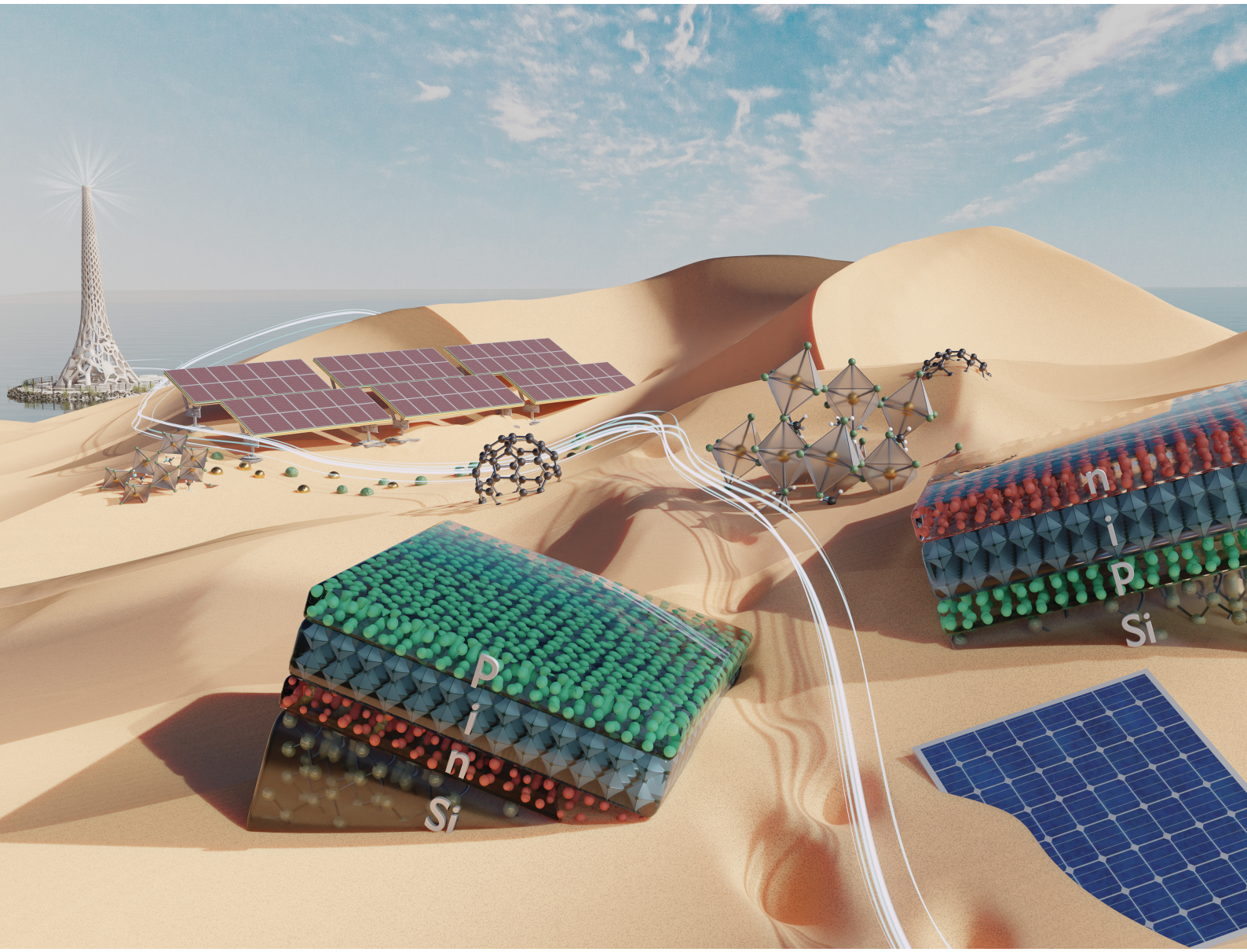

ISSN 1754-5706

ROYAL SOCIETY OF CHEMISTRY

COMMUNICATION

Erkan Aydin, Stefaan De Wolf *et al.*
Ligand-bridged charge extraction and enhanced quantum efficiency enable efficient n–i–p perovskite/silicon tandem solar cells

Energy & Environmental Science

ROYAL SOCIETY OF CHEMISTRY

COMMUNICATION

View Article Online
View Journal | View Issue

Check for updates

Cite this: *Energy Environ. Sci.*, 2021, **14**, 4377

Received 22nd April 2021,
Accepted 30th June 2021

DOI: 10.1039/d1ee01206a

rsc.li/ees

Open Access Article. Published on 30 June 2021. Downloaded on 2/11/2026 11:11:57 PM.
This article is licensed under a Creative Commons Attribution 3.0 Unported Licence.

Ligand-bridged charge extraction and enhanced quantum efficiency enable efficient n–i–p perovskite/silicon tandem solar cells†

Erkan Aydin,*[a] Jiang Liu,[a] Esma Ugur,[a] Randi Azmi,[a] George T. Harrison,[a] Yi Hou,[b] Bin Chen,[b] Shynggys Zhumagali,[a] Michele De Bastiani,[a] Mingcong Wang,[a] Waseem Raja,[a] Thomas G. Allen,[a] Atteq ur Rehman,[a] Anand S. Subbiah,[a] Maxime Babics,[a] Aslihan Babayigit,[ac] Furkan H. Isikgor,[a] Kai Wang,[a] Emmanuel Van Kerschaver,[a] Leonidas Tsetseris,[d] Edward H. Sargent,[b] Frédéric Laquai[a] and Stefaan De Wolf*[a]

Translating the high power conversion efficiencies of single-junction perovskite solar cells in their classic, non-inverted (n–i–p) architecture to efficient monolithic n–i–p perovskite/silicon tandem solar cells with high current densities has been a persistent challenge due to the lack of low-temperature processable, chemically-insoluble contact materials with appropriate polarity and sufficient optical transparency. To address this, we developed sputtered amorphous niobium oxide (a-NbO_x) with ligand-bridged C_{60} as an efficient electron-selective contact, deposited on the textured-silicon bottom cell. For the sunward, hole-selective contact we implemented a stack of molecularly doped broadband transparent evaporated 2,2′,7,7′-tetra(*N*,*N*-di-*p*-tolyl)amino-9,9-spirobifluorene (spiro-TTB) and atomic layer deposited vanadium oxide, which further enhances the device quantum efficiency. Combining these contact materials with two-dimensional perovskite passivation on the micrometer-thick solution-processed perovskite top cell yields 27% efficient monolithic n–i–p perovskite/silicon tandem solar cells, which represents one of the highest power conversion efficiencies reported on pyramidal textured crystalline silicon bottom cells, and the highest with this polarity.

Broader context

Monolithic perovskite/silicon tandem solar cells are of interest thanks to their high power conversion efficiency potential at affordable cost. Also, the possibility to fabricate silicon heterojunction bottom cells either in the n–i–p or p–i–n polarity provides considerable flexibility to choose the device architecture. The initial perovskite/silicon tandems were in the n–i–p configuration. However, as in this architecture light enters from the p-side, the application of the typical electron and hole selective contacts of single-junction devices to the tandem configuration resulted in devices with a poor blue response, in particular due to parasitic absorption in the front-contact stack. Therefore, global tandem research refocused on the inverted structure (p–i–n configuration, with electron collection at the front), and so far, several efficient devices have been reported in this configuration. Increasingly the power conversion efficiency of p–i–n tandems further is constrained by parasitic absorption and recombination active defects in the front SnO_x/C_{60} electron selective layer stack, prompting us to revisit the n–i–p structure with the aim to benefit from the wide library of efficient hole selective layers in single-junction n–i–p perovskite solar cells. In this work, we systematically overcome the persistent challenges of n–i–p tandem devices by developing novel electron and hole selective contact stacks, fully processed on industry-standard textured silicon bottom cells. Our work enables a new device platform and research avenues to further push the efficiency of perovskite-based tandem solar cells.

Introduction

Metal halide perovskite solar cells (PSCs) have been reported with many different material combinations and device configurations. However, in silicon-based tandem architectures, most of the studies in literature have been in the p–i–n configuration.[1–8] Although single-junction n–i–p devices have systematically proven higher power conversion efficiencies (PCEs),[9–11] their translation to the perovskite/silicon tandem configuration has been hindered by (i) a lack of low-temperature processable, chemically insoluble, and conformal electron-selective layers (ESLs), (ii) a lack of efficient, conformal, and optically transparent hole-selective contact stacks, and (iii) an inability to fabricate the perovskite top cell on micron-sized pyramidal textured interfaces, as employed in high-efficiency silicon solar cells.[12] These challenges have limited the performance of n–i–p tandems to ~22% (>1 cm^2)

[a] *King Abdullah University of Science and Technology (KAUST), KAUST Solar Center (KSC), Physical Sciences and Engineering Division (PSE), Thuwal 23955-6900, Kingdom of Saudi Arabia. E-mail: erkan.aydin@kaust.edu.sa, stefaan.dewolf@kaust.edu.sa*
[b] *University of Toronto, Department of Electrical and Computer Engineering, Toronto, Ontario M5S 1A4, Canada*
[c] *Hasselt University, Institute for Materials Research (IMO), Wetenschapspark 1, 3590 Diepenbeek, Limburg, Belgium*
[d] *National Technical University of Athens, Department of Physics, GR15780 Athens, Greece*

† Electronic supplementary information (ESI) available. See DOI: 10.1039/d1ee01206a

Open Access Article. Published on 30 June 2021. Downloaded on 2/11/2026 11:11:57 PM.
This article is licensed under a Creative Commons Attribution 3.0 Unported Licence.

on silicon heterojunction (SHJ) cells, and ~24% (1 cm^2) on poly-silicon passivating-contact silicon solar cells,[13] even though all initial perovskite/silicon tandems were in the n–i–p configuration.[14–17]

In the single-junction n–i–p configuration, several well-established ESLs are available, such as the archetypal compact and mesoporous titanium dioxide (c-TiO_2/m-TiO_2) stack, which requires a high-temperature sintering step (>450 °C), however.[11,18,19] This temperature requirement excludes the applicability of this ESL stack for tandems built onto high-performance SHJ bottom cells,[20] whose temperature processing window is <250 °C due to their amorphous-silicon passivated surfaces. Thin films of tin oxide nanoparticles (np-SnO_x) are also increasingly used as an ESL on PSCs,[21] and these are usually deposited at lower temperatures (<200 °C).[22,23] However, np-SnO_x ESLs are solution-processed. As a result, achieving conformal deposition on rough, complex surfaces, such as pyramidal-textured silicon, is difficult. Furthermore, thermally-evaporated C_{60} is a successful ESL, but is soluble by subsequent perovskite solution processing.

In the search for alternative ESLs, thin-film niobium pentoxide (Nb_2O_5) stands out as it combines favorable properties such as a low work function (WF), a wide bandgap, high chemical and ultraviolet (UV) light stability, as well as compatibility with various processing techniques.[24–28] To adopt such Nb_2O_5 layers to n–i–p tandems as an ESL, we employed the RF-sputtering technique. Using stoichiometric targets under an argon atmosphere, we achieved a slightly oxygen (O) deficient and amorphous film structure. Notably, we find that such O vacancies in the amorphous phase do not induce deep-level trap states, in contrast to np-SnO_x, but rather act as shallow donor-like defects that improve the conductivity and mobility in the bulk of the film, and promote charge extraction through the contact structure. Modification of the charge transport layer/perovskite interface with C_{60} derivatives is a successful strategy to further enhance electron extraction.[29–32] To apply this at a-NbO_x/perovskite interface, we utilize C_{60} with a functionalized pyrrolidine tail to create a conformal self-assembled molecular monolayer (SAM), anchored on the a-NbO_x surface, which makes it insoluble to the aprotic solvents used in perovskite solution processing. To support our findings, we theoretically underpin this self-anchoring interaction by density functional theory (DFT) calculations. On the device-level, we show high PCE values for both perovskite single-junction and perovskite/silicon tandem solar cells utilizing C_{60}-anchored a-NbO_x ESLs, thanks to reduced non-radiative recombination at the interface.

Another major factor hindering the progress of n–i–p tandems has been the lack of efficient, optically transparent, and conformal hole selective layers (HSLs) and buffer layers. Such buffer layers protect the soft perovskite absorber from sputter damage during the deposition of the top transparent conductive oxide (TCO). In the more widespread p–i–n tandem configuration, a bilayer consisting of an evaporated C_{60} ESL, followed by an ALD SnO_x buffer layer, is employed, onto which a TCO is sputtered. So far, the most widely reported HSL for n–i–p devices is spiro-OMeTAD, but this material suffers from strong parasitic absorption in the blue part of the solar spectrum, and requires post oxidation with metal–organic complexes for improved hole mobility.[33] Nevertheless, several thermally evaporable small-molecule HSLs could be used.[34,35] However, the common issue with these molecules is their low hole mobility, low electrical conductivity, and unfavorable ionization potential.[36] To address this, we evaporated small molecule HSLs [2,2′,7,7′-tetra(*N*,*N*-di-*p*-tolyl)amino-9,9-spirobifluorene (spiro-TTB)[2] and *N*4,*N*4,*N*4″,*N*4″-tetra([1,1′-biphenyl]-4-yl)-[1,1′:4′,1″-terphenyl]-4,4″-diamine (TaTm)[37]] and doped them using the strong electron-accepting molecule 2,2′-(perfluoronaphthalene-2,6-diylidene) dimalononitrile (F6-TCNNQ)[38] to enhance the hole mobility and conductivity. Finally, we tested these HSLs in bilayer stacks with vanadium oxide (VO_x)[39] and tungsten oxide (WO_x) as buffer layers, first in single-junction devices, and then in monolithic perovskite/silicon tandems. On our optimized devices, we used doped spiro-TTB/VO_x bilayers as an HSL stack.

To minimize reflection losses from the silicon bottom cells,[1–3,7,8] we utilized textured SHJ bottom cells, onto which micrometer-thick perovskites were solution-processed. In addition, we utilized a mixed 2D/3D passivation treatment on the perovskite top surface for improved charge extraction, and reduced hysteresis, which have been implemented usually in n–i–p configuration devices to date. Combining minimized reflection losses with reduced parasitic absorption by evaporated HSLs enabled one of the highest PCEs for tandems on textured interfaces. Combined, these systematic improvements in the n–i–p tandem device design solve the persistent issues that have hindered their progress on SHJ bottom cells, resulting in an improvement in PCE from ~22%[17] to over 27%, a performance that is commensurate with its state-of-the-art p–i–n tandem counterparts.

Characteristics of pristine and C_{60}-anchored a-NbO_x films

Scanning electron microscope (SEM) and atomic force microscopy (AFM) top-view images reveal the amorphous morphology of our sputtered NbO_x films (Fig. 1a and Fig. S1c, respectively, ESI†). Unlike spin-casted np-SnO_x films (Fig. S1b, ESI†), our a-NbO_x films show a high conformality on the textured-Si surface, which is critical for tandem integration (Fig. 1b). High-resolution transmission electron microscopy (HR-TEM) (Fig. 1c), and surface-sensitive grazing incidence X-ray diffraction (GIXRD) measurements of a-NbO_x films (Fig. 1d) confirm the amorphous nature of the material. In addition, post-deposition annealing of the films at elevated temperature (up to 500 °C) does not lead to crystal formation, as shown by the XRD graphs in the inset figure of Fig. 1d.[40]

The multi-valent nature of niobium (Nb) leads to various stable oxidation states (+2, +4 and +5), resulting in different polymorphs such as NbO, NbO_2, and Nb_2O_5.[41] Here, our amorphous films are sputtered from a Nb_2O_5 target in a pure Ar atmosphere (without intentional oxygen flow), yielding nearly stoichiometric Nb_2O_5 films, which is thermodynamically the most stable phase.[42] Nevertheless, our a-NbO_x films are

 This journal is © The Royal Society of Chemistry 2021

Open Access Article. Published on 30 June 2021. Downloaded on 2/11/2026 11:11:57 PM.
This article is licensed under a Creative Commons Attribution 3.0 Unported Licence.

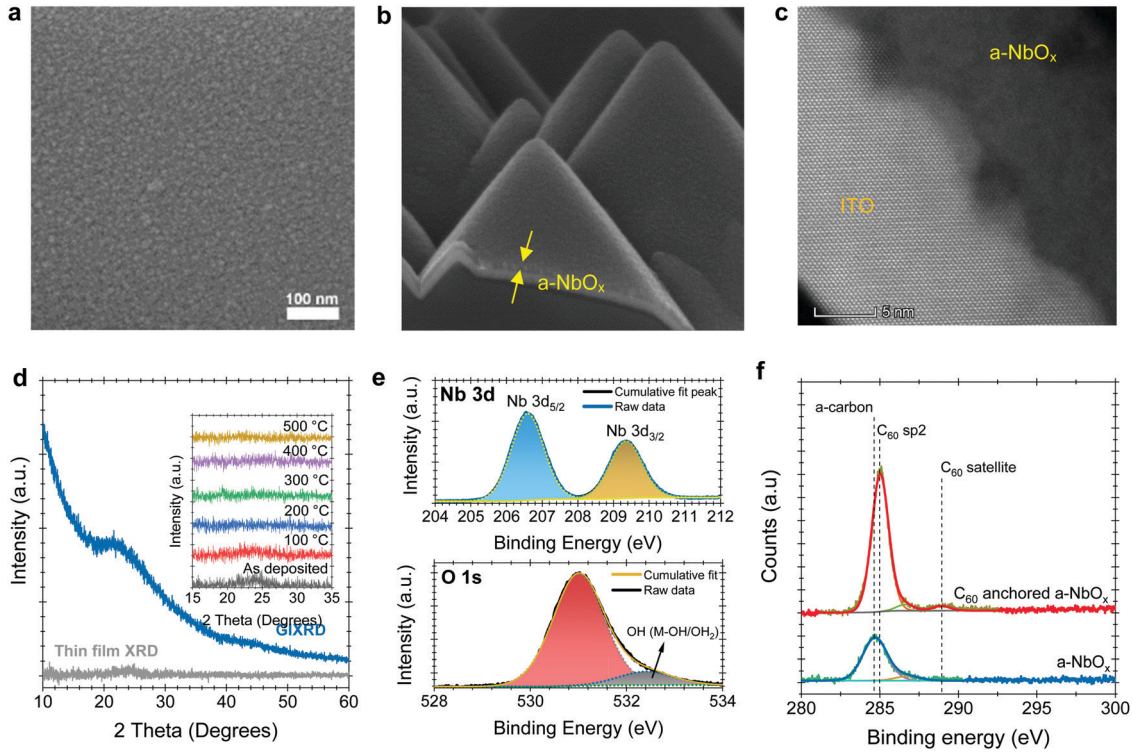

Fig. 1 SEM images of the a-NbO_x films (a) on soda-lime glass substrates and (b) on textured crystalline silicon. (c) Cross-sectional HR-TEM image of the a-NbO_x films deposited on crystalline ITO. (d) XRD graph of the a-NbO_x films with powder XRD and GIXRD analysis, which does not reveal any prominent peak. The inset figure in panel d shows the powder XRD of the films post-annealed at different temperatures. HR-XPS spectra of the (e) Nb 3d, and O 1s states of a-NbO_x films together with (f) XPS spectra of a-NbO_x and C_{60}-anchored a-NbO_x films.

slightly O-deficient, according to our X-ray photoelectron spectroscopy (XPS) analysis (Note S1, ESI†). The O-deficient character of the a-NbO_x films is further demonstrated by a two orders of magnitude decrease in electrical conductivity of the films after annealing in ambient air (Note S2, ESI†).[40,43] We investigate the chemical structure of the a-NbO_x (Fig. 1e) and np-SnO_x (Fig. S2, ESI†) films using high-resolution XPS spectra, which show that Nb ions exist in single metal-oxide environments of Nb^{5+} with Nb 3d 5/2 (207.3 eV). The elemental composition of the films by wide survey XPS scans (Fig. S2a and b, ESI†) revealed an atomic percentage ratio of $Nb/O_{metaloxide}$ = 1/2.2 and $Sn/O_{metaloxide}$ = 1/1.8 for a-NbO_x and np-SnO_x, respectively (see Note S1, ESI† for a detailed analysis). These results indicate a slightly O-deficient nature of the films, resulting in improved conductivity. We confirm the C_{60}-anchoring on a-NbO_x layers *via* XPS analysis, as the metal oxide core lines are strongly attenuated with a concomitant increase in the peak at ~284.7–285 eV, corresponding to C_{60} sp^2 carbon (Fig. 1f). The increased peak intensity further indicates efficient coverage of the C_{60}–SAM molecule on a-NbO_x films, as discussed in detail in Note S1 (ESI†).

Based on DFT calculations, we find a strong energetic preference for the O vacancies of a-NbO_x to aggregate at the (100) surface of a particular crystal polymorph, which was employed as an approximate description of the material (as explained in the Note S3, ESI†). As a result, C_{60}-pyrrolidine molecules can self-assemble on this surface by forming bonds between pyrrolidine terminating O and the surface Nb sites. On the other hand, the C_{60} moiety interacts with the perovskite. The contact angle on a-NbO_x films reveals that the surface becomes more hydrophobic after C_{60}-anchoring; the AFM-measured roughness remains the same, suggesting conformal coverage (Fig. S8 and S1c, respectively, ESI†). C_{60}-anchored random-pyramid textured silicon wafers also show hydrophobicity, which indicates good coverage over this complex surface (Fig. S8, ESI†).

The measured WF, valence band maximum (VBM), and conduction band minimum (CBM) of the a-NbO_x layers, determined by ultraviolet photoelectron spectroscopy (UPS), analysis are −4.32 eV, −7.50 eV, and −3.85 eV (VBM + E_g) from the vacuum, respectively (see Note S4, ESI†). This suggests that the a-NbO_x Fermi level is located close to its CBM, indicative of its strong n-type character. The relative band edges and WF values of all the layers in single-junction and tandem devices are shown in Fig. S9 (ESI†). We estimate the optical band gap (E_g; derived from Tauc plots) of the a-NbO_x films is 3.65 eV, which is sufficiently high to be applied as an ESL in PSCs (Fig. S11c and d, ESI†).

Single-junction solar cells with C_{60}-anchored a-NbO_x

To investigate the performance of the C_{60}-anchored a-NbO_x layers as ESL, we first fabricated single-junction n–i–p PSCs based on triple-cation perovskites (1.61 eV),[44,45] as sketched in

Open Access Article. Published on 30 June 2021. Downloaded on 2/11/2026 11:11:57 PM.
This article is licensed under a Creative Commons Attribution 3.0 Unported Licence.

Fig. 2a. Photoluminescence (PL) images reveal increased phase homogeneity (Fig. 2b) while SEM and XRD results confirm the high-crystallinity of the perovskite layer (Fig. S12a and b, ESI†) on C_{60}-anchored a-NbO_x. The J–V characteristics of the fabricated devices (with np-SnO_x layers as a control) are shown in Fig. 2c. As reported in Table S4 (ESI†), C_{60}-anchored a-NbO_x based devices reach a 21.3% PCE for a 1.61 eV perovskite absorber, with high batch-to-batch reproducibility and negligible hysteresis (Fig. S13, ESI†).

Taking the advantage of low parasitic absorption of a-NbO_x layers, ESL-side illuminated single-junction devices show a high short-circuit current density (J_{SC}) of 24 mA cm^{-2}, which is higher than their np-SnO_x-based counterparts. These results are confirmed by external quantum efficiency (EQE) measurements, as shown in Fig. 2d (23.3 mA cm^{-2} from the integrated current density from EQE, within a 5% margin of equipment error). The average statistical distribution of the J_{SC} results also confirms this observation, as shown in Fig. S13 (ESI†). Spectrally weighted absorptance values reveal that C_{60}-anchored a-NbO_x and np-SnO_x has negligible absorption within the 290–850 nm range (0.65 and 1.02 W m^{-2} nm^{-1}, respectively). $1 - R$ (R is reflectance) measurements from the whole device stack show that the PSCs based on such stacks suffer from similar R losses (112.6 and 116.9 W m^{-2} nm^{-1}, respectively). In conclusion, high J_{SC} values is mainly due to efficient charge collection as evidenced by EQE measurements (Fig. 2d).

Further, C_{60}-anchored a-NbO_x devices provide ~4% absolute higher fill factor (FF) values on average compared to C_{60}-anchored np-SnO_2 counterparts. To understand this difference, we simulated the electric-field distribution across the device profile, which is governed by the built-in voltage (V_{bi}), with different biasing voltages, as discussed in Note S6 (ESI†). Considering that the perovskite/HSL interface is identical for all cases, the low voltage drop at this interface can be attributed to a high shunt and low contact resistivity of the overall stack and a higher V_{bi} (Fig. S15, ESI†). In an ideal case, the charge separation process is evidently more efficient if the internal electric field is stronger. Accordingly, we observed that a-NbO_x based devices show a higher electric-field ratio between the ESL/perovskite and the perovskite/HSL interface, and overall lower voltage losses at the perovskite/HSL interface (see Fig. S16, ESI†). This implies an improved contact quality at the ESL/perovskite interface, which we assign to the high negative fixed-charge density of a-NbO_x.[46] C_{60}-anchoring further improves the electric-field ratio and provides effective passivation at the perovskite/ESL interface.[32] The relatively lower diode ideality factor of a-NbO_x based devices (n = 1.23)

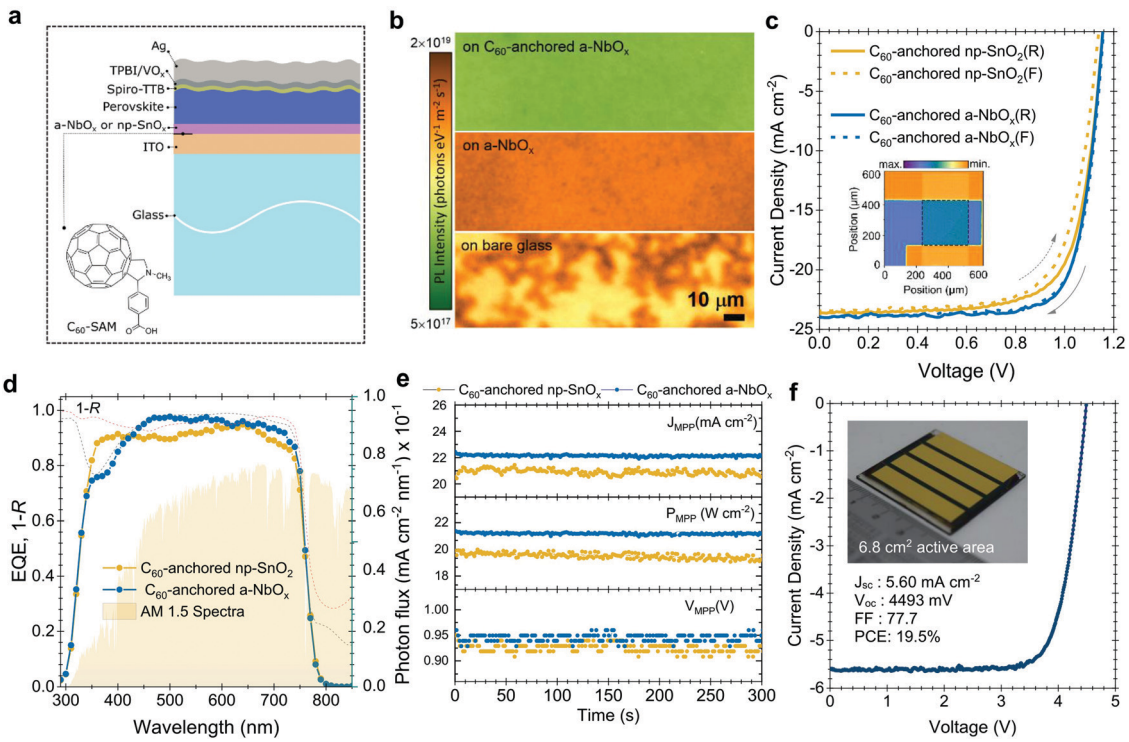

Fig. 2 (a) Device architecture of single-junction PSCs with the chemical structure of the SAM molecule used in this study. (b) PL images of the perovskite layers on various ESL substrates. (c) J–V characteristics of the champion single-junction PSCs for np-SnO_x and a-NbO_x based devices and (d), corresponding EQE spectra (the dashed lines represents the 100 − R data). Note that the devices results here are reported with magnesium fluoride antireflection layer on glass side. In panel (c), the marked area in the inset image shows the LBIC image of the 0.1 cm^2 PSCs. (e) MPP tracking of the np-SnO_x and a-NbO_x based PSCs at room temperature by using a three-point perturbation method. (f) J–V characteristics of the mini-module based on four series-connected cells. The inset fig. in panel (f) shows the photograph of the rear side of the mini-module. Note that all reported perovskite absorbers in this figure have 1.61 eV bandgap.

 This journal is © The Royal Society of Chemistry 2021

Open Access Article. Published on 30 June 2021. Downloaded on 2/11/2026 11:11:57 PM.
This article is licensed under a Creative Commons Attribution 3.0 Unported Licence.

than that of np-SnO_x-based devices (n = 1.35) suggests that in the former case the recombination occurs predominantly in the quasi-neutral region rather than in the space-charge region of the device. (Fig. S18, ESI†). Here, the high negative fixed-charge density of a-NbO_x may enhance the drift region in ESL/perovskite devices, which in turn leads to enhanced charge extraction and less recombination. We attribute this behavior to the high dipole moment at the a-NbO_x/perovskite interface. Specifically, C_{60}–SAM anchoring on the a-NbO_x surface increases the negative charge density at the ESL/perovskite interfaces which leads to a further increases in dipole moment and electric field (see Note S6, ESI†).

Surprisingly, the FF values of the devices are not significantly affected by increasing the thickness of the a-NbO_x layers up to 75 nm (Fig. S14, ESI†). Typically, metal oxide-based charge transport layers give the best PCE values when their thickness is limited to $<$30 nm due to their poor conductivity.[47–50] We hypothesize that the absence of deep-level defect states in the bulk of the a-NbO_x films, together with its thickness-independent high negative fixed-charge density allows the use of thicker films. Indeed, DFT calculations of the electronic density of states (DOS) as a function of energy demonstrate that O vacancies do not create states within the bandgap of a-NbO_x. Instead, the defects shift the highest occupied states at the bottom of the CBM of the material, resulting in enhanced n-type conductivity (Note S3, ESI†). In contrast, O vacancies in tetragonal np-SnO_x introduce energy levels within the bandgap of the material (Fig. S7, ESI†) and can thus act as carrier trap sites. All these results underline the efficient electron selective character of the C_{60}-anchored a-NbO_x films.

Differences between the reverse (V_{OC} to J_{SC}) and forward (J_{SC} to V_{OC}) scan are a persistent problem of the n–i–p PSCs. The potential reasons for such observed hysteresis in the case of our devices are investigated in detail in Note S8 (ESI†). More generally, we mitigated this issue by balancing the charge extraction speed at both ends of the contacts by implementing 2D/3D passivation on top of the perovskite surface (*i.e.* hole-collecting side), and C_{60}-anchoring to the a-NbO_x (*i.e.* electron-collecting side), as well as improving the perovskite crystallinity by using urea as an additive. We verified our results with stabilized power output values measured by the three-point perturbation MPP tracking method (see algorithm in Note S7, ESI†), shown in Fig. 2e (21.3% for a-NbO_x and 19.9% for the np-SnO_x based devices). Finally, we demonstrate the implementation of large-area deposited C_{60}-anchored a-NbO_x layers by fabricating a mini-module with a 6.8 cm^2 active area, which consists of four series-connected cells. The mini-module delivered a PCE of 19.5% (active area) with a FF of 77.7%, (the J–V curve is shown in Fig. 2f), demonstrating the scalability of the C_{60}-anchored a-NbO_x layers.[51]

Perovskite/silicon tandem solar cells on double-side textured silicon cells

We fabricated micrometer-thick perovskite films *via* solution processing on the C_{60}-anchored a-NbO_x ESL (see processing details in Fig. S21, ESI†). The high perovskite crystal quality and uniformity is evidenced by the high spatial uniformity of the current collection from the tandem devices by light-beam-induced-current (LBIC) imaging (Fig. 3a). As can be seen from the cross-sectional SEM images in Fig. 3b, the perovskite layer has full end-to-end coverage on the micron-scale pyramids

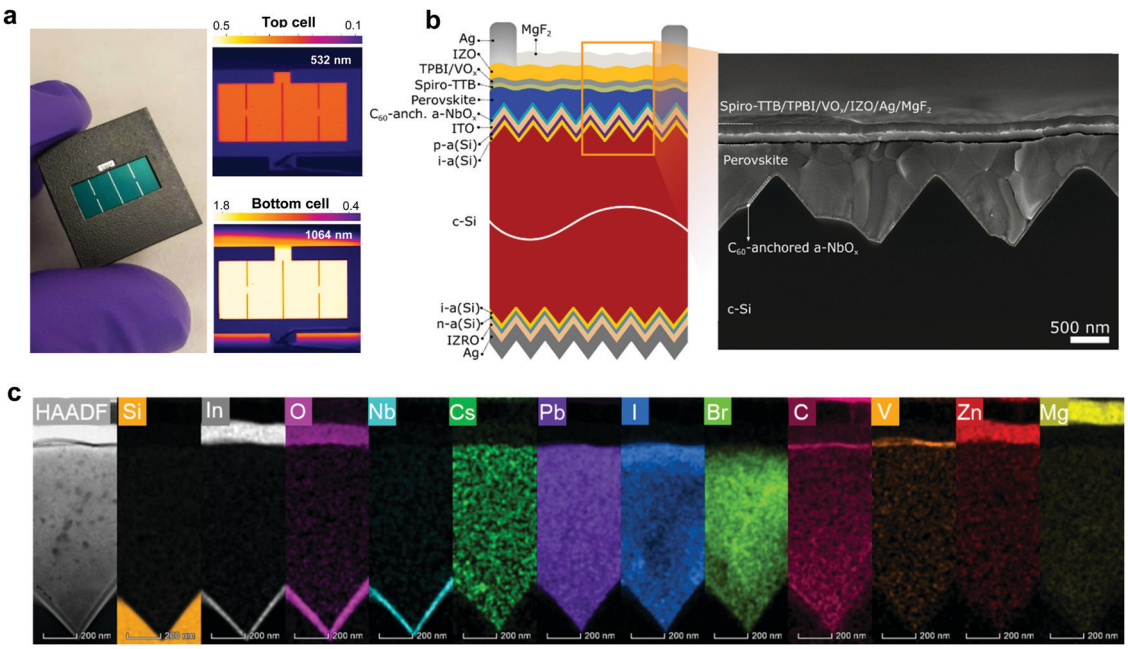

Fig. 3 (a) The masked photograph, and LBIC images of the perovskite/silicon tandem solar cells with an excitation wavelength of 532 and 1064 nm. The scale bar shows the signal intensity. (b) Schematic of the device architecture with SEM cross-section view. (c) HRTEM images and EDX elemental mapping of the representative elements for each layer of the fabricated stack.

Open Access Article. Published on 30 June 2021. Downloaded on 2/11/2026 11:11:57 PM.
This article is licensed under a Creative Commons Attribution 3.0 Unported Licence.

without leaving any uncovered pyramid or void at the interface. We verified the homogenous distribution of the perovskite elements by energy-dispersive X-ray spectroscopy (EDX) mapping from a slice of cross-sectional TEM images shown in Fig. 3c. Notably, by utilizing large-area uniform sputtered a-NbO_x ESLs (as shown in Fig. S22, ESI†) with self-anchored C_{60}, we eliminated the chemical solubility challenge of the ESL during perovskite processing as shown in Fig. S23 (ESI†). The carboxylic-acid-terminated anchoring group of the C_{60}–SAM interacts with the a-NbO_x surface thanks to its strong affinity and prevents the washing away of the C_{60} layer during the perovskite deposition.[52] Also, the high lateral resistivity of the a-NbO_x film impedes the flow of shunt currents on textured interfaces.

For the HSLs, we first tested conventional Li-doped spiro-OMeTAD but expectedly, this resulted in considerable parasitic absorption in the range of 300-430 nm and a modest tandem J_{SC} of 17.5 mA cm^{-2} (see Fig. S24, ESI†) due to its considerable required thickness (conventionally ~150 nm) (Fig. 4a). To circumvent this issue, we used thermally evaporated, conformal, and thin HSLs such as spiro-TTB (~25 nm) and TaTm (~50 nm). Here, we successfully adopted a strong electron acceptor dopant, F6-TCCNQ to the evaporated HSLs (host), which is evident from the absorption peak in the 450–570 nm range (see Fig. S25a, ESI†) – due to the π–π*-transition of the cations/charge transfer (CT) states within the HSL.[53,54] The overall parasitic absorption of the optimally doped HSLs is much less than for conventional spiro-OMeTAD (Fig. 4a). The observed near infrared (NIR) absorption peak of the spiro-TTB at ~950 nm can be attributed to the F6-TCNNQ anion; this peak is not seen for TaTm.[55] However, TaTm strongly absorbs in the blue and limits the response of the perovskite subcell (Fig. 4a). Table 1 summarizes the device characteristics of the single-junction PSC (based on 1.68 eV) with various ESLs. Upon

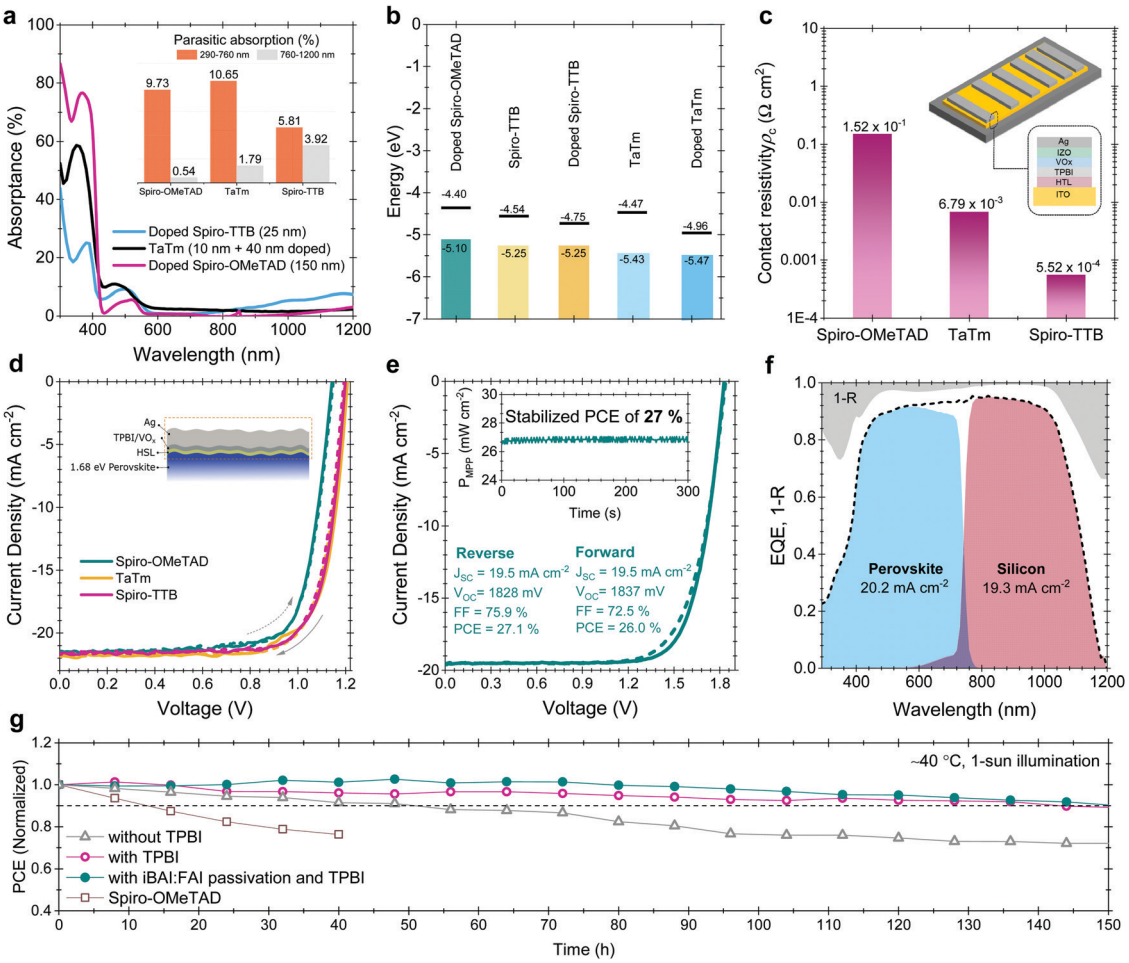

Fig. 4 (a) Absorptance spectra of the doped spiro-OMeTAD, spiro-TTB and TaTm HSLs used in the devices. The inset figure shows the parasitic absorption of the layers at different wavelength range. We choose 760 nm as a crossover point of subcells. (b) The WF and VBM values of the various HSLs used in this study and (c) contact resistivity values for top contact stacks with these HSLs. The inset figure shows the sketch of the TLM contact pads and the contact stack. (d) Corresponding *J*–*V* curves based on 1.68 eV single-junction perovskites from glass side illumination. (e) *J*–*V* curve of the perovskite/silicon tandems and (f) corresponding EQE of this device. The gray shaded area in the EQE graph shows the 1 − *R* data. The inset graph in e represents the stabilized device parameters achieved by the MPP tracking method. (g) 150 h T_{90} stability results of glass/glass encapsulated tandems under 1-sun continuous illumination and *J*–*V* scans at every 8 hours. Between the measurements the devices were kept at MPP voltage with the three-point perturbation method. During the stability measurements, devices were kept at ~40 °C as explained in Fig. S34 (ESI†).

 This journal is © The Royal Society of Chemistry 2021

Open Access Article. Published on 30 June 2021. Downloaded on 2/11/2026 11:11:57 PM. This article is licensed under a Creative Commons Attribution 3.0 Unported Licence.

doping, the ionization potential of the HSLs is shifted down as shown in Fig. 4b and this leads to an increased V_{OC}. Overall, with these improvements, using doped spiro-TTB, we fabricated n–i–p tandems with higher perovskite subcell J_{SC} values (20.2 mA cm^{-2} by EQE) compared to their p–i–n counterparts (19.1 mA cm^{-2}) (Note S11, ESI†) with V_{OC} values of >1.8 V.

We found that a-NbO_x does not induce a considerable contact resistivity as confirmed by the *J–V* curves of the SHJ bottom cells and the contact resistivity values by transmission line measurements (TLM, see Fig. S27, ESI†), which facilitates high FF values. Also, among various HSL stacks, spiro-TTB-based ones give the lowest contact resistivity, as shown in Fig. 4c. The *J–V* characteristics of the single-junction devices for various HTLs (Fig. 4d) and monolithic tandems with optimized spiro-TTB are shown in Fig. 4e which shows high batch-to-batch reproducibility (see Fig. S28, ESI†). Notably, we enhance the NIR response of the tandems by reducing the reflection losses owing to the double-side textured nature of the SHJ bottom cells (Fig. S29, ESI†). To balance the J_{SC} of top and bottom cells, we use a 1.68 eV bandgap perovskite obtained by increasing the Br percentage from 15% to 25%, which is in the range of an ideal top cell bandgap.[1] To minimize the hysteresis behavior, which is discussed in Note S8 (ESI†), we utilized a mixed 2D/3D passivation treatment strategy (see structural details in Fig. S30, ESI†) since this enables non-continuous 2D layers on the perovskite surface by passivating the surface defects, while still allowing charge transport *via* 3D perovskite pathways. By applying iso-butylammonium iodide, (iBAI) and formamidinium iodide (FAI) mixed passivation, we decreased the number of surface defects and mitigated ion migration, thereby significantly decreasing the hysteresis of the device (see Fig. 4e and Fig. S31, ESI†).[56]

Furthermore, we minimized the parasitic absorption losses in the blue range of the solar spectrum by combining thermally-evaporated spiro-TTB with atomic layer deposited VO_x in the hole selective contact stack (see discussion on buffer layer selection in Note S13, ESI†) as well as by replacing the rear ITO with Zr-doped indium oxide (IZRO)[57] (for a lower extinction coefficient) and by thinning down the front indium zinc oxide (IZO) from 100 to 70 nm (Fig. S33, ESI†). As a consequence of improved light management (Fig. 4f), combined with enhanced charge extraction, we record a significant improvement from the last reported perovskite/silicon tandem in the n–i–p configuration on a SHJ bottom cell (which was ~22%) and achieved a 27% efficient monolithic tandem performance from such devices, which is one of the highest PCEs reported in either the n–i–p (see Table S7, ESI†) or p–i–n tandem configurations.[2–5] We confirmed this PCE value by MPP measurements under continuous illumination (inset of Fig. 4e).

We also performed stability tests of the tandem devices under 1-sun continuous illumination and intermittent *J–V* scans. For this, we first encapsulated devices between two glass sheets with butyl rubber as edge sealant, shown in Fig. S34 (ESI†). The optimized devices maintained 90% of their initial V_{OC} and FF values for 150 h (Fig. 4g). In the literature, n–i–p devices are frequently reported to have short operational stability due to fast degradation of the doped HSL.[33,36,37] To identify potential degradation mechanisms of our HSL stacks, we performed a set of stability measurements. We found that the spiro-TTB/VO_x interface appears to be sensitive to degradation due to Lewis acid quenching of radical anions and di-anions of the F6-TCNNQ, with a consequence of the free electron lone pairs that act as a Lewis base. At the HSL/VO_x interface, vanadium centers act as a Lewis acid, and attract and coordinate highly electron-rich nitrogen atoms of F6-TCNNQ, thereby suppressing its activity. From our stability test with single-junction test structures, we found that elevated temperature is the primary reason for this accelerated degradation (see Fig. S35, ESI†). This stems from the accumulation of quenched dopants at the VO_x interface at elevated temperature.[58] To mitigate this issue, we introduced a 2 nm thin layer of 2,2′,2″-(1,3,5-Benzinetriyl)-tris(1-phenyl-1-*H*-benzimidazole), TPBI, which effectively prevented the interaction between F6-TCNNQ and VO_x without jeopardizing the charge transfer due its ultra-thin nature.

Table 1 The summary of the device performances of 1.68 eV based single-junction PSCs with various HSLs after 2D/3D passivation

HSL	Scan direction	V_{OC} (mV)	J_{SC} (mA cm^{-2})	FF (%)	PCE (%)
Spiro-OMeTAD	V_{OC} to J_{SC}	1142	21.4	76.5	18.8
	J_{SC} to V_{OC}	1148	21.6	75.5	18.8
TaTm	V_{OC} to J_{SC}	1208	21.8	75.1	19.7
	J_{SC} to V_{OC}	1201	21.9	75.4	19.8
Spiro-TTB	V_{OC} to J_{SC}	1200	21.6	76.6	19.8
	J_{SC} to V_{OC}	1193	21.7	76.6	19.8

Efficient charge extraction at C_{60}-anchored a-NbO_x and perovskite interfaces

We performed time-resolved photoluminescence (TRPL) spectroscopy measurements to analyze the charge carrier dynamics at the perovskite/ESL interface. We found that the PL lifetime of the perovskite in the quartz/a-NbO_x/perovskite sample is significantly longer than that of both the quartz/np-SnO_x/perovskite and the quartz/perovskite sample structure (Fig. 5a). We note that the substrate could affect the perovskite film formation and thereby the perovskite defect distribution which in turn could alter the PL lifetime of the perovskite films, as shown in Fig. 2b. We hypothesize that the reason for the longer PL lifetime is two-fold: (i) the absence of deep-level defects at the a-NbO_x/perovskite interface, and (ii) the dependency of the PL lifetime of the absorber on the carrier concentration (N_e) of the charge transport layers, where low N_e values lead to less quenching of the PL lifetime.[19,59] Here, compared to np-SnO_x, a-NbO_x films have a seven orders of magnitude lower carrier concentration than np-SnO_x, which appears to be the reason for this behavior (Table S1, ESI†).

We note that the PL lifetime of C_{60}-anchored a-NbO_x/perovskite sample is almost three times that of the C_{60}-anchored np-SnO_x/perovskite sample. The shorter PL lifetime of the latter can be caused by either efficient charge extraction from the perovskite to the ESL or increased recombination at the

Open Access Article. Published on 30 June 2021. Downloaded on 2/11/2026 11:11:57 PM.
This article is licensed under a Creative Commons Attribution 3.0 Unported Licence.

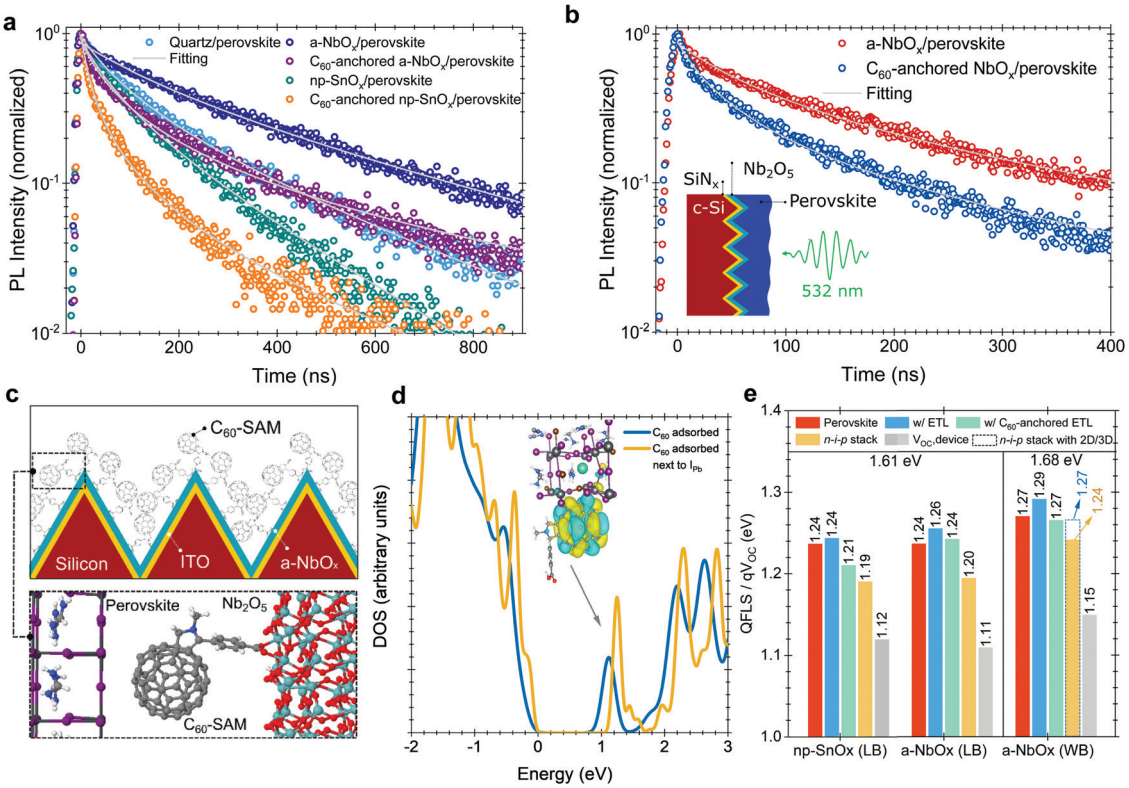

Fig. 5 The PL decay of (a) 1.61 eV perovskite samples on quartz, (b) 1.68 eV perovskites on textured c-Si/SiN_x substrates. The decays were probed at ~768 and ~738 nm across a ~20 meV range for 1.61 and 1.68 eV perovskites, respectively. All the samples were excited at 532 nm with a fluence 0.5 μJ cm^{-2} and a repetition rate of 1 kHz. (c) Schematics of the self-assembly process. The magnified area shows the proposed model for the interaction of the pyrrolidine group of a C_{60}–SAM molecule with a-NbO_x and the electronic coupling of C_{60} molecule with perovskite lattice. (d) Electronic density of states (DOS) for the structure shown in I and for C_{60} molecule physisorbed on a Pb–I terminated perovskite surface with and without an Pb–I anti-site defect. The zero energy is at the valence band maximum of the perovskite. Peaks shown with arrow points out C_{60}-related empty states in the bandgap. (Nb: dark gray, O:red, C: gray, N: blue, H:white, Pb: dark orange, I: purple, Br: dark gray, Cs: cyan spheres). (e) QFLS values of perovskite and perovskite/transport layer stacks, and V_{OC} values of the devices for 1.61 eV and 1.68 eV bandgap perovskites. Values extracted from the absolute PL data using a hyperspectral imaging system with the excitation at 532 nm under 1-sun illumination condition (LB: low bandgap, WB: wide bandgap).

interface.[19] To clarify the origin, we determined the k_1 values, which are related to trap-assisted recombination, for samples with and without C_{60}-anchored ESLs. We found that C_{60}-anchoring on np-SnO_x and a-NbO_x resulted in lower k_1 values than observed for neat ESLs and overall less trap-assisted recombination. All values are listed in Table 2.

To evidence the C_{60}-anchoring on the a-NbO_x films on textured substrates, we performed TRPL measurements also on wide bandgap (1.68 eV) perovskite absorbers deposited on textured c-Si/SiN_x/perovskite stacks, where SiN_x is silicon nitride, which is used to electrically isolate the Si wafer (Fig. 5b). Here, we found the PL lifetime to be reduced from 140 ns to 57 ns in the case of C_{60}-anchoring, confirming the enhanced charge extraction properties of the self-assembled layer on textured interfaces, which is in line with the measurements performed on the 1.61 eV bandgap perovskites on quartz substrates.

For the C_{60}–SAM anchoring, the pyrrolidine group of the C_{60}–SAM molecule strongly interacts with the metal oxide ESLs (Fig. 5c), while its C_{60} component interacts with (negatively-charged) iodide ions, which originate from non-coordinated Pb or Pb–I anti-site defects. To further elaborate on the role of the

Table 2 The PL decay rate constants of the perovskite samples determined by TRPL. Excitation of the samples was incident on the quartz side

Sample	k_1 (s^{-1})	k_2 (cm^3 s^{-1})	t (ns)
Quartz/perovskite (1.61 eV)	2.8×10^6	2.2×10^{-10}	172
Quartz/a-NbO_x/perovskite (1.61 eV)	1.8×10^6	8.1×10^{-11}	384
Quartz/C_{60}-anchored a-NbO_x/perovskite (1.61 eV)	1.0×10^6	4.3×10^{-10}	107
Quartz/np-SnO_x/perovskite (1.61 eV)	4.4×10^6	2.7×10^{-10}	130
Quartz/C_{60}-anchored np-SnO_x/perovskite (1.61 eV)	2.6×10^6	1.3×10^{-9}	36
Textured c-Si/SiN_x/a-NbO_x/perovskite (1.68 eV)	1.8×10^6	2.5×10^{-10}	140
Textured c-Si/SiN_x/C_{60}-anchored a-NbO_x/perovskite (1.68 eV)	1.8×10^6	6.7×10^{-10}	57

 This journal is © The Royal Society of Chemistry 2021

Open Access Article. Published on 30 June 2021. Downloaded on 2/11/2026 11:11:57 PM.
This article is licensed under a Creative Commons Attribution 3.0 Unported Licence.

C_{60}–SAM cage, we modeled the adsorption of such a cage (with and without the pyrrolidine tail) on the (001) surface of formamidinium lead iodide ($FAPbI_3$), as well as on the (001) surface of a mixed perovskite of the composition $FA_{0.70}MA_{0.20}Cs_{0.10}PbI_{2.50}Br_{0.50}$ with DFT calculations. In these cases, the fullerene moiety physisorbed on the perovskite (with a significant binding energy of about 1.79 eV for C_{60} on $FAPbI_3$), creating empty energy states inside the energy bandgap of the $FAPbI_3$. It should be noted that, in the $FA_{0.70}MA_{0.20}Cs_{0.10}PbI_{2.50}Br_{0.50}$ case, the C_{60}-related state is also below a gap level associated with the common Pb–I anti-site perovskite defect.

In agreement with experiments, our DFT calculations (Note S3, ESI†) suggest that the empty C_{60}-related gap states can extract electrons from the conduction band or electron traps (related to, *e.g.*, Pb–I antisite defects) of the perovskite (Fig. 5d) and pass them on to the NbO_x side through the firmly attached pyrrolidine tails. On the ESL side, the role of O vacancies (O_v) is crucial for the efficient extraction of electrons. In the SnO_x case, O_v defects create charge trap states (Fig. S7, ESI†) that can hinder carrier transport, which is in line with space-charge-limited-current (SCLC) and impedance spectroscopy measurements (Note 14 and 15, ESI†). On the other hand, in the NbO_x case, O_v shifts the highest occupied states into the bottom of the conduction band. This effect is also found for O-deficient NbO_x terminations (Fig. S6, ESI†), and persists even after C_{60}-anchoring. At this level of theory, O_v enhances the n-type conductivity of the material, in agreement with the aforementioned experimental observations.

To support our V_{OC} results, we performed absolute PL measurements (Fig. S38, ESI†) to determine the quasi-Fermi-level-splitting (QFLS), which represents the maximum achievable V_{OC} from the perovskite absorbers with and without contact stacks. Herein, C_{60}-anchored a-NbO_x based stacks show 1.24 eV, while np-SnO_x devices show 1.21 eV for 1.61 eV perovskites (Fig. 5e), in line with the results of the TRPL measurements (Fig. 5a), and also the V_{OC} values of the devices (Table S4, ESI†). The presence of the C_{60}-anchoring improves the charge extraction in both a-NbO_x and np-SnO_x samples but it lowers the QFLS values due to energetic issues, as discussed in Note S4 (ESI†). However, in devices, the measured V_{OC} values are lower than the QFLS values. According to our measured UPS and IPES data, both a-NbO_x and np-SnO_x layers add a 20 meV potential barrier at the interface to perovskite after C_{60}-anchoring. However, several studies reported that this level of CB offset is needed to suppress interfacial recombination due to the reduced back-transfer recombination and improved FF.[60–62]

Conclusion and outlook

Here, we overcome the persistent processing limitations of n–i–p configuration perovskite/silicon tandem solar cells by combining on pyramidal textured SHJ bottom cells a RF-sputtered a-NbO_x with conformal C_{60}-anchoring as ESL, micrometer-thick solution-processed perovskites and a highly transparent conformal HSL stack. All these advancements enabled 27% efficient perovskite/silicon monolithic tandems in n–i–p configuration, which is a $>5\%$ absolute increment over the prior state of the art on SHJ bottom cells. Our demonstration of an efficient n–i–p tandem device platform opens new pathways to propel the efficiency of perovskite/silicon tandems beyond the thermodynamic limit for single-junction solar cells. For instance, thermally-evaporated C_{60} ESL for p–i–n configuration stands out unrivaled so far, even though this material causes strong parasitic absorption. On the other hand, there are many small molecule HSLs in the literature which have remained unexplored in n–i–p tandem solar cells to improve the device optics further and overall reaching to >20 mA cm^{-2} tandem devices. Furthermore, to overcome the limited long-term operational stability of the perovskite/silicon tandems, 2D-perovskite passivation strategies can be utilized which has been a challenge with p–i–n devices due to energetic alignment problems of the 2D perovskites with the widely used C_{60} ESLs. Also, bifacial tandem devices can be more relevant in the n–i–p configuration, since the bottom cell utilizes an n-type contact at its back, high refractive index but lower conductivity TCOs can be utilized. Beyond these opportunities, our developed hole selective contact stack will also enable progress in perovskite/perovskite tandems by eliminating the air exposure requirement of moisture-sensitive Sn-based perovskites during HSL processing, which has been an issue so far. Lastly, the n–i–p tandem platform enables utilization of tandems as a photocathode in efficient solar-driven water splitting applications for hydrogen generation since this application requires electrons to be extracted from the cathode side with voltage values of >1.4–1.8 V, as well as high current densities.

Experimental section

Deposition of a-NbO_x and np-SnO_2 layers

a-NbO_x layers were deposited by radio frequency (RF, 13.56 MHz) magnetron sputtering from the stoichiometric a-NbO_x target (Plasmaterials, 99.95% purity) at room temperature using Angstrom Engineering EvoVac system at 1.97 W cm^{-2} power density. The Argon gas was supplied to the chamber with 20 sccm. The deposition rate of the films was 0.15 Å s^{-1}. The base pressure for deposition was $<2 \times 10^{-6}$ Torr, and the deposition pressure was 3 mTorr. Before each deposition, the target was pre-sputtered for 10 min to remove the contamination layer, if any, on the surface of the target. For homogenous deposition, substrate rotation was provided. The substrate was not heated or cooled intentionally. np-SnO_2 layers were deposited by spin-casting of aqueous Alfa Aesar nanoparticle suspension at 3000 rpm for 30 s (with 3000 rpm s^{-1} ramp rate), and resultant films were annealed in ambient air at 150 °C for 30 min. Prior to np-SnO_x deposition, 10 min UV-ozone treatment was applied on ITO/glass substrates. However, this step was not used prior to the deposition of a-NbO_x layers.

Open Access Article. Published on 30 June 2021. Downloaded on 2/11/2026 11:11:57 PM.
This article is licensed under a Creative Commons Attribution 3.0 Unported Licence.

C_{60}–SAM modification of a-NbO_x layers

C_{60}-based self-assembled monolayer (C_{60}-COOH-SAM, CAS No.: 631918-72-4, Luminescence Technology Corp.) dissolved in chlorobenzene and stirred vigorously overnight. Later, the stock solution filtered using a 0.2 μm PTFE filter. The C_{60}–SAM was spun on a-NbO_x or np-SnO_x at 3000 rpm for 60 s with a 3000 rpm s^{-1} ramp rate. Before this, the surface of the a-NbO_x layer is treated with 1 mg mL^{-1} concentrated aqueous potassium chloride solution.

Fabrication of the single junction perovskite solar cells

The mixed $Cs_{0.05}MA_{0.15}FA_{0.8}Pb(I_{0.85}Br_{0.15})_3$ perovskite precursor solution was prepared using FAI (0.96 M), MABr (0.18 M), CsI (0.06 M) PbI_2 (1.04 M), and $PbBr_2$ (0.185 M) materials in a mixed solvent of 800 μL DMF and 200 μL DMSO. The perovskite solution was spin-coated on electron transport layers (either 20 nm np-SnO_x or 50 nm a-NbO_x) at two-step: 2000 rpm for 10 s and 4000 rpm for 30 s. For antisolvent quenching, 150 μl chlorobenzene was dropped through the center of the substrates 10 s prior to the end of the spin-coating process. After that, films were transferred immediately onto 100 °C preheated hotplate and annealed for 30 min. 25 nm Spiro-TTB was deposited by thermal evaporation as defined below. 10 nm ALD deposited vanadium oxide (VO_x) was deposited using *via* the Picosun ALD tool using vanadyl-tri-isopropoxide (VTIP, precursor was kept 80 °C) and H_2O as precursors and substrate at 90 °C. 100 nm of Ag layers were thermally evaporated on top of HSL stack by thermal evaporation in an Angstrom Engineering EvoVac deposition system. 100 nm of MgF_2 is evaporated (if stated) as an anti-reflective layer with 1 Å s^{-1} deposition rate to minimize the reflection losses for both np-SnO_x and a-NbO_x layers.

Fabrication of the silicon bottom cell

SHJ bottom cells are fabricated on float-zone double-side-textured four inches wafers (n-doped, resistivity 1–5 Ω cm^{-1}, thickness 250–280 μm). The texturing process is done in an alkaline solution to get randomly distributed pyramids and cleaned in RCA1 and RCA2 solution. The size of the pyramids is controlled by adjusting the alkaline concentration and the process temperature. Before the PECVD depositions, the wafers are dipped in 5% hydrofluoric acid solution to remove the native oxide layer. The intrinsic, p, and n silicon amorphous layers are deposited in a PECVD cluster (Indeotec Octopus – 2) with a thickness of 8, 6, and 13 nm, respectively. The back electrode is realized by sputtering sequentially ITO and Ag (150 and 250 nm, respectively) in the PVD part of the Octopus cluster. In case of IZRO rear TCO, the recipe given in our previous publication is used.[57] The ITO recombination junction (15 nm) is sputtered in the same tool. Prior to the a-NbO_x deposition, and after a-NbO_x deposition, the wafers are annealed at 190 °C for 10 min to recover the sputtering damage.

Fabrication of the perovskite top cell

To achieve n–i–p configuration perovskite top cells, a-NbO_x layers (20 nm on the textured surface) is deposited by RF sputtering as the ESL and modified by C_{60}–SAM as defined above. Before C_{60}–SAM deposition the samples were annealed at 190 °C in glove box for 20 min to mitigate the plasma damage on the bottom cells. On top, the $Cs_{0.05}MA_{0.15}FA_{0.8}Pb(I_{0.75}Br_{0.25})_3$ perovskite is deposited from a 1.7 M solution in DMF : DMSO (4 : 1) *via* 3-step spin coating process (see Note S9 for details, ESI†). For better crystallization, we added 0.25 mg mL^{-1} urea (Merck) to the precursor as we introduced previously.[63] To prepare 2D/3D mixed passivation solution, iBAI and FAI (and other organohalides such as MAI, MACl) was mixed in isopropyl alcohol with total solution concentration of 10 mM. Here, the iBAI and FAI wt ratio in solution 3 : 1. After dissolving, the solutions were filtered with PTFE filters (0.2 mm) and spin casted on previously fabricated perovskite films (at room temperature) at 5000 rpm for 20 s. No annealing step was applied. 25 nm Spiro-TTB (Lumtec, Sublimed, >99%, in alumina crucible) and F6-TCNNQ (Lumtec, >99%) were cosublimed at 260–280 °C and 160–170 °C, respectively by the Angstrom EvoVac evaporation system. The deposition rate was controlled by QCM sensors and adjusted to obtain the desired doping concentrations. For the host materials (spiro-TTB and TaTm, here TaTm is from TCI) the deposition rate was 0.8 Å s^{-1} in alumina crucible. The optimal dopant evaporation rate was 0.1 Å s^{-1}, which represents the 11.1 wt% doping ratio. HSLs were capped with 2 nm of thermally evaporated TPBI (Ossila, Unsublimed >98.0%, 0.2 Å s^{-1}, in alumina crucible), and 10 nm VO_x is deposited by ALD as defined above. 70 or 100 nm IZO top electrode was sputtered in the Angstrom EvoVac sputtering system with an RF of 42 W at (60 and 40 Ω sq^{-1}, repsectively), as defined in the text. 350 nm Ag contacts were evaporated through a shadow mask using Angstrom EvoVac thermal evaporator with 2.5 Å/s deposition rate. Finally, 120 nm of MgF_2 is evaporated with the same equipment as an anti-reflective layer with 1 Å s^{-1} deposition rate. Device layouts are given in Fig. S39 (ESI†).

Characterization of the photovoltaic performances

Single junction PSCs and tandem solar cells were tested under standard test conditions (100 mW cm^{-2}, AM1.5G, 25 °C). Single junction PSCs were tested with ABET Technologies Sun 3000 Solar Simulator equipped with Keithley 2400 source meter. The light intensity was calibrated using a certified reference cell with a KG5 filter (RERA Solutions, calibrated at Radboud University Nijmegen). Devices were tested at a 200 mV s^{-1} scan rate. Devices had a 0.1 cm^2 square active area (as shown in the inset of Fig. 2c). Note that the reverse scan is from V_{OC} to J_{SC} (1.25 V → −0.1 V), and the forward scan is from J_{SC} to V_{OC} (−0.1 V → 1.25 V). No preconditioning protocol has been used before the measurement.

J–V measurements of the tandem solar cells were performed using Wavelabs Sinus 220 LED-based solar simulator. To calibrate spectrum, we used Fraunhofer ISE certified calibration cell (without a filter). We did not apply a spectral mismatch factor. The illumination area of the devices was 1.03 cm^2, which is determined by the laser cut shadow mask coated with black paint. Maximum power point tracking (MPPT) measurements

 This journal is © The Royal Society of Chemistry 2021

Open Access Article. Published on 30 June 2021. Downloaded on 2/11/2026 11:11:57 PM.
This article is licensed under a Creative Commons Attribution 3.0 Unported Licence.

were performed *via* the homemade LabView® based software using a three-point weight comparison method (for details, see Note S7, ESI†). The device measurements were performed at 200 mV s^{-1} scan speed. EQE measurements were performed using PV-Tools LOANA equipment. When measuring perovskite top cells, the tandem devices were light-biased by IR LEDs (930 nm); when measuring silicon bottom cells, the tandem devices were light-biased by a blue LED to saturate the subcells. To enable the near short-circuit conditions, MPP voltages were applied on the devices. All device characterizations were performed at ambient air with RH ~50% and without any encapsulation.

Stability tests

Devices were encapsulated between two glasses (3 mm low iron glasses) with 10 mm wide and 1 mm thick butyl rubber Solargain® edge sealant with desiccant (Quanex, SET LP03), which were laminated at 100 °C. The illuminated area (1 cm^2) of the cells was determined by non-transparent black tape on top of the front glasses. Indoor stability measurements were performed with Lot Oriel class AAA solar simulator equipped with a Xenon lamp. The encapsulated modules were kept at 25 °C cooled by refrigerated circulation stage. For MPP tracking measurements, devices were kept under MPP load *via* a three-point perturbation method, and *J-V* scans were performed every three hours.

Structural and optical characterizations

Atomic force microscopy (AFM) images were obtained with tapping mode using a Digital Instruments Multimode AFM (Veeco Metrology Group). A probe (TAP150A, Veeco) with a force constant of ~5 N m^{-1} was used. X-ray diffraction patterns were obtained using a Bruker D8 Advance X-ray diffractometer ($CuK_{\alpha 1}$ radiation, λ = 1.5406 Å) from 10° to 80° (2θ) with a scan speed of 3° min^{-1}. The Scanning transmission electron microscopy (STEM) images were taken by an FEI Themis-Z transmission electron microscope operated at 300 kV. Energy Dispersive X-ray Spectroscopy studies were performed with a Bruker super-X EDS detector. TEM lamellas were prepared on an FEI Helios G4 FIB/SEM dual-beam system equipped with a Ga+ ion source. C/Pt layers were deposited on the surface region of interest by the Electron & Ion beam for sample protection. Samples were thinned down to a relative thickness of 80 nm using progressively decreasing ion beam energies in the FIB down to 5 keV. Contact angles were measured with a KRUSS-The Drop Shape Analyzer DSA100 system by using water as the wetting solvent. Spectroscopic ellipsometry measurements of the a-NbO_x/c-Si stacks were performed by using J. A. Woollam M-2000DI at 65° and 75°. The c-Si substrate was a single-polished float-zone wafer (525 ± 25 mm), and a-NbO_x film was deposited on the polished side. Such a substrate can effectively impede interference caused by light reflection from the rear side. An optical model of air/surface roughness/ a-NbO_x/c-Si is used to fit the (Y,D) raw data. The impedance measurements were performed on Fluxim Paios system.

UPS/XPS analysis

All the films were prepared on pre-cleaned ITO substrates as used in devices. The measurements were carried out with a UHV 0.5–1 10^{-9} mbar *Omicron* spectrometer equipped with a monochromatic Al K_α X-ray *Omicron* XM1000 X-ray source ($h\nu$ = 1486.6 eV) operating at 389 W and a Sphera II spectrometer with a 7-channel channeltron. The survey and high-resolution spectra were collected at constant analyzer pass energies (CAE) of 50 and 15 eV, respectively. Samples (~0.5 × 1.0 cm) were mounted in electrical contact to the *Omicron* style sample plate by clamping with Ta clips in contact with the sample surface, binding energy calibration and sample charging were accounted for by reference to the ambient contamination C 1s adventitious carbon, ~284.7 eV. Samples were introduced to the chamber *via* a N_2 filled UHV compatible transfer system from an N_2 glove box where the samples were mounted to minimize ambient exposure. The spectra were analyzed with Casa XPS software. The individual peak envelopes were fitted by a Gaussian (70%)–Lorentzian (30%) (GL30) function after Shirley-type background subtraction. UPS measurements were performed in the same instrument on the same samples with a (CAE) of 10 eV, using a He (I) excitation discharge lamp ($h\nu$ = 21.22 eV) (Focus). A bias of −9.97 V was applied to the sample. The photoelectrons were collected at an angle of 90° between the sample and analyzer.

Time-resolved photoluminescence (TR-PL) spectroscopy

Perovskite films were deposited either on pre-cleaned quartz substrates or on ESLs (np-SnO_x and a-NbO_x) using the same recipe as used for device fabrication. After deposition of the layers, samples were placed in a sealed N_2 chamber to avoid any changes due to photo-induced degradation. All measurements were performed at room temperature. The samples were excited with the Coherent Helios 532 nm nanosecond (ns) laser with a pulse width of 0.85 ns and a peak with a repetition rate of 1 kHz. The excitation beam at 532 nm was focused on pumping the samples, mounted inside the sealed chamber. The PL of the samples was collected by an optical telescope (consisting of two plano-convex lenses) and focused on the slit of a spectrograph (PI Spectra Pro SP2300) and detected with a Streak Camera (Hamamatsu C10910) system. The data was acquired in photon counting mode using the Streak Camera software (HPDTA). The photogenerated carrier concentration at t = 0 was calculated using the formula[64] of $n_0 = \alpha \cdot f / E_{photon}$ where α is the absorption coefficient at the excitation wavelength, f is the fluence of the laser and E_{photon} is the excitation photon energy. The PL lifetimes were determined by using the general rate equation $(-dn/dt = k_1 n + k_2 n^2)$ however, excluding Auger recombination, since the initial carrier concentration was low ($n_0 = 4 \times 10^{16}$ cm^{-3}), where Auger recombination is negligible in perovskites.[65]

Absolute PL measurements

Perovskite films were deposited on pre-cleaned glass substrates or on ESLs (np-SnO_x and a-NbO_x) using the same recipe as used for device fabrication. The absolute PL spectra of the samples

Open Access Article. Published on 30 June 2021. Downloaded on 2/11/2026 11:11:57 PM.
This article is licensed under a Creative Commons Attribution 3.0 Unported Licence.

were collected using a hyperspectral imaging system coupled to a microscope with 2 nm spectral resolution (Photon *etc.* IMA). Samples were excited with 532 nm laser at ~1 sun illumination condition (before the measurement, the power density of the laser was adjusted with a reference perovskite solar cell). The absolute calibration procedure of the setup is reported in detail elsewhere.[66] The collected data was analyzed *via* home-built MatLab code using modified generalized Plank law to get quasi-Fermi level splitting using the formula:[67]

$$\varphi_{(E,\theta)} = A_{(E,\theta)}\frac{\cos\theta}{4\pi^3 h^3 {c_0}^2}E^2\frac{1}{\exp\left(\frac{E-\Delta\mu}{k_B T}\right)-1}$$

where $A_{(E,\theta)}$ is the absorption probability of a photon with energy E, incident at an angle θ with respect to the surface normal. $\Delta\mu$ and k_BT are quasi-Fermi level splitting and Boltzmann constant and the temperature (equivalent to 25.7 meV at room temperature), respectively. Here, $\cos\theta$ factor appears as the emission from the surface following Lambert's law.

Device simulations

The optical response of the single-junction PSCs was calculated based on the finite element method (COMSOL Multiphysics), where periodic boundary conditions were implemented in a unit cell.[68] The linearly polarized plane wave was illuminated normally to the cell top surface. The PSC was illuminated from the top with a linearly polarized plane wave impinging normally to the cell top surface, covering the wavelength ranges from 300 nm to 800 nm (AM1.5G illumination), comprising the bandgap of PSCs. Two-dimensional device simulation of NbO_x and SnO_x PSCs was based on a classical drift-diffusion and Poisson's equation and solved by the finite element method (COMSOL Multiphysics) based semiconductor device simulator.[69] The simulation was carried out at 300 K under one sun (AM1.5G, −100 mW cm^{-2}) condition. The optical bandgap, thickness, and energetics (bandgaps, electron affinity) related to the active and other layers used in the simulation were obtained from the UPS/IPES measurements and listed in Note S4 (ESI†).

DFT analysis

Calculations were performed with the DFT code Quantum Espresso,[70] the Perdew–Wang generalized-gradient approximation exchange-correlation functional (xc),[71] projector-augmented waves,[72] [3] and the DFT-D2 method[73] to include van der Waals interactions. The energy cutoff for the plane-wave basis was set at 100 Rydbergs. The calculation of densities of states (DOS) employed the Monkhorst–Pack scheme with Gaussian broadening and 4 × 4 × 1 *k*-grids.[74] In total energy calculations on large supercells, only the gamma point was used for *k*-sampling. Structures were rendered with VESTA.[75] To model O vacancies in the bulk of SnO_2 and Nb_2O_5 we used supercells with, respectively, 71 and 111 atoms. The calculations pertaining to adsorption of pyrrolidine or C_{60}-pyrrolidine on the (001) surface of SnO_x, the (100) surface of Nb_2O_5, and the (001) surface of the halide perovskite used supercell slabs with, respectively, 102, 142, and 197 atoms. The large size of the supercells precluded the possibility of using post-DFT corrections in the form of a hybrid xc-functional.

Author contributions

E. A. conceived the idea, designed the experiments, fabricated the devices, and conducted device characterizations, and performed optoelectronic characterizations of the fabricated layers. E. A., Y. H., M. D. B., and B. C. developed the wide-bandgap perovskite processing on textured interfaces. E. U. optimized the C_{60}–SAM process, contributed to HSL optimizations, and performed TRPL and absolute PL (using hyperspectral imaging system) measurements and data analysis. E. U, R. A, and S. Z. contributed to the single-junction device fabrication. M. W. developed MPP tracking software and MatLab code for quasi-Fermi level splitting calculations and contribute to data analysis. F. L. supervised TRPL and absolute PL spectroscopy measurements and data analysis. L. T. performed the DFT calculations. W. R. performed two-dimensional device simulations. J. L. contributed the single-junction device fabrication and optimized the 1.61 eV perovskite absorbers, performed AFM measurements. M. D. B. performed OPAL simulations and transient photocurrent measurements. A. B. joined data interpretation of the hysteresis behavior and band levels of the layers. F. H. I. performed contact angle and SCLC measurements. A. S. S. performed the impedance analysis. F. H. I. and A. S. S. designed the mini-module contact layout. E. A. designed the tandem device contact layout. K. W. performed the XRD measurements. G. T. H. performed XPS, UPS, and IPES measurements. T. G. A., M. D. B., A. U. R., M. B. and E. V. K. fabricated the silicon bottom cells. E. A. composed the manuscript. All authors discussed the results and commented on the manuscript. S. D. W., F. L., and E. H. S. supervised the project.

Conflicts of interest

The authors declare no competing interests.

Acknowledgements

The authors would like to thanks to Nini Wei for the TEM images; funding: the research reported in this publication was supported by funding from King Abdullah University of Science and Technology (KAUST) under award no. OSR-CARF/CCF-3079 and award no. IED OSR-2019-4208.

References

1 E. Aydin, T. G. Allen, M. De Bastiani, L. Xu, J. Ávila, M. Salvador, E. Van Kerschaver and S. De Wolf, *Nat. Energy*, 2020, **5**, 851–859.
2 F. Sahli, J. Werner, B. A. Kamino, M. Bräuninger, R. Monnard, B. Paviet-Salomon, L. Barraud, L. Ding, J. J. Diaz Leon, D. Sacchetto, G. Cattaneo, M. Despeisse,

 This journal is © The Royal Society of Chemistry 2021

Open Access Article. Published on 30 June 2021. Downloaded on 2/11/2026 11:11:57 PM.
This article is licensed under a Creative Commons Attribution 3.0 Unported Licence.

M. Boccard, S. Nicolay, Q. Jeangros, B. Niesen and C. Ballif, *Nat. Mater.*, 2018, **17**, 820–826.

3 Y. Hou, E. Aydin, M. De Bastiani, C. Xiao, F. H. Isikgor, D.-J. Xue, B. Chen, H. Chen, B. Bahrami, A. H. Chowdhury, A. Johnston, S.-W. Baek, Z. Huang, M. Wei, Y. Dong, J. Troughton, R. Jalmood, A. J. Mirabelli, T. G. Allen, E. Van Kerschaver, M. I. Saidaminov, D. Baran, Q. Qiao, K. Zhu, S. De Wolf and E. H. Sargent, *Science*, 2020, **367**, 1135–1140.

4 M. Jošt, E. Köhnen, A. Morales Vilches, B. Lipovšek, K. Jäger, B. Macco, A. Al-Ashouri, J. Krc, L. Korte, B. Rech, R. Schlatmann, M. Topic, B. Stannowski and S. Albrecht, *Energy Environ. Sci.*, 2019, **11**, 3511–3523.

5 J. Xu, C. C. Boyd, Z. J. Yu, A. F. Palmstrom, D. J. Witter, B. W. Larson, R. M. France, J. Werner, S. P. Harvey, E. J. Wolf, W. Weigand, S. Manzoor, M. F. A. M. van Hest, J. J. Berry, J. M. Luther, Z. C. Holman and M. D. McGehee, *Science*, 2020, **367**, 1097–1104.

6 D. Kim, H. J. Jung, I. J. Park, B. W. Larson, S. P. Dunfield, C. Xiao, J. Kim, J. Tong, P. Boonmongkolras, S. G. Ji, F. Zhang, S. R. Pae, M. Kim, S. B. Kang, V. Dravid, J. J. Berry, J. Y. Kim, K. Zhu, D. H. Kim and B. Shin, *Science*, 2020, eaba3433, DOI: 10.1126/science.aba3433.

7 B. Chen, Z. J. Yu, S. Manzoor, S. Wang, W. Weigand, Z. Yu, G. Yang, Z. Ni, X. Dai, Z. C. Holman and J. Huang, *Joule*, 2016, **4**, 850–864.

8 A. S. Subbiah, F. H. Isikgor, C. T. Howells, M. De Bastiani, J. Liu, E. Aydin, F. Furlan, T. G. Allen, F. Xu, S. Zhumagali, S. Hoogland, E. H. Sargent, I. McCulloch and S. De Wolf, *ACS Energy Lett.*, 2020, **5**, 3034–3040.

9 E. Aydin, M. De Bastiani and S. De Wolf, *Adv. Mater.*, 2019, 1900428.

10 J. J. Yoo, G. Seo, M. R. Chua, T. G. Park, Y. Lu, F. Rotermund, Y.-K. Kim, C. S. Moon, N. J. Jeon, J.-P. Correa-Baena, V. Bulović, S. S. Shin, M. G. Bawendi and J. Seo, *Nature*, 2021, **590**, 587–593.

11 J. Jeong, M. Kim, J. Seo, H. Lu, P. Ahlawat, A. Mishra, Y. Yang, M. A. Hope, F. T. Eickemeyer, M. Kim, Y. J. Yoon, I. W. Choi, B. P. Darwich, S. J. Choi, Y. Jo, J. H. Lee, B. Walker, S. M. Zakeeruddin, L. Emsley, U. Rothlisberger, A. Hagfeldt, D. S. Kim, M. Grätzel and J. Y. Kim, *Nature*, 2021, **592**, 381–385.

12 C. Battaglia, A. Cuevas and S. De Wolf, *Energy Environ. Sci.*, 2016, **9**, 1552–1576.

13 H. Shen, S. T. Omelchenko, D. A. Jacobs, S. Yalamanchili, Y. Wan, D. Yan, P. Phang, T. Duong, Y. Wu, Y. Yin, C. Samundsett, J. Peng, N. Wu, T. P. White, G. G. Andersson, N. S. Lewis and K. R. Catchpole, *Sci. Adv.*, 2018, **4**, eaau9711.

14 J. P. Mailoa, C. D. Bailie, E. C. Johlin, E. T. Hoke, A. J. Akey, W. H. Nguyen, M. D. McGehee and T. Buonassisi, *Appl. Phys. Lett.*, 2015, **106**, 121105.

15 J. Werner, L. Barraud, A. Walter, M. Bräuninger, F. Sahli, D. Sacchetto, N. Tétreault, B. Paviet-Salomon, S.-J. Moon, C. Allebé, M. Despeisse, S. Nicolay, S. De Wolf, B. Niesen and C. Ballif, *ACS Energy Lett.*, 2016, **1**, 474–480.

16 S. Albrecht, M. Saliba, J. P. Correa Baena, F. Lang, L. Kegelmann, M. Mews, L. Steier, A. Abate, J. Rappich, L. Korte, R. Schlatmann, M. K. Nazeeruddin, A. Hagfeldt, M. Grätzel and B. Rech, *Energy Environ. Sci.*, 2016, **9**, 81–88.

17 F. Sahli, B. A. Kamino, J. Werner, M. Bräuninger, B. Paviet-Salomon, L. Barraud, R. Monnard, J. P. Seif, A. Tomasi, Q. Jeangros, A. Hessler-Wyser, S. De Wolf, M. Despeisse, S. Nicolay, B. Niesen and C. Ballif, *Adv. Energy Mater.*, 2017, 1701609, DOI: 10.1002/aenm.201701609.

18 M. Jeong, I. W. Choi, E. M. Go, Y. Cho, M. Kim, B. Lee, S. Jeong, Y. Jo, H. W. Choi, J. Lee, J.-H. Bae, S. K. Kwak, D. S. Kim and C. Yang, *Science*, 2020, **369**, 1615–1620.

19 J. Peng, J. I. Khan, W. Liu, E. Ugur, T. Duong, Y. Wu, H. Shen, K. Wang, H. Dang, E. Aydin, X. Yang, Y. Wan, K. J. Weber, K. R. Catchpole, F. Laquai, S. De Wolf and T. P. White, *Adv. Energy Mater.*, 2018, **0**, 1801208.

20 M. De Bastiani, A. S. Subbiah, E. Aydin, F. H. Isikgor, T. G. Allen and S. De Wolf, *Mater. Horiz.*, 2020, **7**, 2791–2809.

21 C. Altinkaya, E. Aydin, E. Ugur, F. H. Isikgor, A. S. Subbiah, M. De Bastiani, J. Liu, A. Babayigit, T. G. Allen, F. Laquai, A. Yildiz and S. De Wolf, *Adv. Mater.*, 2021, **33**, 2005504.

22 Q. Jiang, Y. Zhao, X. Zhang, X. Yang, Y. Chen, Z. Chu, Q. Ye, X. Li, Z. Yin and J. You, *Nat. Photonics*, 2019, **13**, 460–466.

23 T. Bu, J. Li, F. Zheng, W. Chen, X. Wen, Z. Ku, Y. Peng, J. Zhong, Y.-B. Cheng and F. Huang, *Nat. Commun.*, 2018, **9**, 4609.

24 X. Ling, J. Yuan, D. Liu, Y. Wang, Y. Zhang, S. Chen, H. Wu, F. Jin, F. Wu, G. Shi, X. Tang, J. Zheng, S. Liu, Z. Liu and W. Ma, *ACS Appl. Mater. Interfaces*, 2017, **9**, 23181–23188.

25 Z. Wang, J. Lou, X. Zheng, W.-H. Zhang and Y. Qin, *ACS Sustainable Chem. Eng.*, 2019, **7**, 7421–7429.

26 W.-Q. Wu, J.-F. Liao, J.-X. Zhong, Y.-F. Xu, L. Wang and J. Huang, *Angew. Chem., Int. Ed.*, 2020, **132**, 21166–21173.

27 S. L. Fernandes, L. G. S. Albano, L. J. Affonço, J. H. D. da Silva, E. Longo and C. F. D. O. Graeff, *Front. Chem.*, 2019, **7**, 50.

28 B. Macco, L. E. Black, J. Melskens, B. W. H. van de Loo, W.-J. H. Berghuis, M. A. Verheijen and W. M. M. Kessels, *Sol. Energy Mater. Sol. Cells*, 2018, **184**, 98–104.

29 M. Zhang, Q. Chen, R. Xue, Y. Zhan, C. Wang, J. Lai, J. Yang, H. Lin, J. Yao, Y. Li, L. Chen and Y. Li, *Nat. Commun.*, 2019, **10**, 4593.

30 S. Wang, H. Chen, J. Zhang, G. Xu, W. Chen, R. Xue, M. Zhang, Y. Li and Y. Li, *Adv. Mater.*, 2019, **31**, 1903691.

31 A. Abrusci, S. D. Stranks, P. Docampo, H.-L. Yip, A. K. Y. Jen and H. J. Snaith, *Nano Lett.*, 2013, **13**, 3124–3128.

32 C. Xiao, C. Wang, W. Ke, B. P. Gorman, J. Ye, C.-S. Jiang, Y. Yan and M. M. Al-Jassim, *ACS Appl. Mater. Interfaces*, 2017, **9**, 38373–38380.

33 K. Rakstys, C. Igci and M. K. Nazeeruddin, *Chem. Sci.*, 2019, **10**, 6748–6769.

34 L. E. Polander, P. Pahner, M. Schwarze, M. Saalfrank, C. Koerner and K. Leo, *APL Mater.*, 2014, **2**, 081503.

35 R. A. Belisle, P. Jain, R. Prasanna, T. Leijtens and M. D. McGehee, *ACS Energy Lett.*, 2016, **1**, 556–560.

36 T. H. Schloemer, J. A. Christians, J. M. Luther and A. Sellinger, *Chem. Sci.*, 2019, **10**, 1904–1935.

Open Access Article. Published on 30 June 2021. Downloaded on 2/11/2026 11:11:57 PM. This article is licensed under a Creative Commons Attribution 3.0 Unported Licence.

37 C. Momblona, L. Gil-Escrig, E. Bandiello, E. M. Hutter, M. Sessolo, K. Lederer, J. Blochwitz-Nimoth and H. J. Bolink, *Energy Environ. Sci.*, 2016, **9**, 3456–3463.
38 F. Zhang and A. Kahn, *Adv. Funct. Mater.*, 2018, **28**, 1703780.
39 J. A. Raiford, R. A. Belisle, K. A. Bush, R. Prasanna, A. F. Palmstrom, M. D. McGehee and S. Bent, *Sustainable Energy Fuels*, 2019, **3**, 1517–1525.
40 R. A. Rani, A. S. Zoolfakar, A. P. O'Mullane, M. W. Austin and K. Kalantar-Zadeh, *J. Mater. Chem. A*, 2014, **2**, 15683–15703.
41 I. Nowak and M. Ziolek, *Chem. Rev.*, 1999, **99**, 3603–3624.
42 K. T. Jacob, C. Shekhar, M. Vinay and Y. Waseda, *J. Chem. Eng. Data*, 2010, **55**, 4854–4863.
43 M. A. Aegerter, *Sol. Energy Mater. Sol. Cells*, 2001, **68**, 401–422.
44 K. Wang, M.-C. Tang, H. X. Dang, R. Munir, D. Barrit, M. De Bastiani, E. Aydin, D.-M. Smilgies, S. De Wolf and A. Amassian, *Adv. Mater.*, 2019, **31**, 1808357.
45 H. X. Dang, K. Wang, M. Ghasemi, M.-C. Tang, M. De Bastiani, E. Aydin, E. Dauzon, D. Barrit, J. Peng, D.-M. Smilgies, S. De Wolf and A. Amassian, *Joule*, 2019, **3**, 1746–1764.
46 B. Macco, M. Bivour, J. H. Deijkers, S. B. Basuvalingam, L. E. Black, J. Melskens, B. W. H. van de Loo, W. J. H. Berghuis, M. Hermle and W. M. M. Kessels, *Appl. Phys. Lett.*, 2018, **112**, 242105.
47 Q. Jiang, L. Zhang, H. Wang, X. Yang, J. Meng, H. Liu, Z. Yin, J. Wu, X. Zhang and J. You, *Nat. Energy*, 2017, **2**, 16177.
48 E. Ugur, A. D. Sheikh, R. Munir, J. I. Khan, D. Barrit, A. Amassian and F. Laquai, *ACS Energy Lett.*, 2017, **2**, 1960–1968.
49 E. Aydin, J. Troughton, M. De Bastiani, E. Ugur, M. Sajjad, A. Alzahrani, M. Neophytou, U. Schwingenschlögl, F. Laquai, D. Baran and S. De Wolf, *ACS Appl. Energy Mater.*, 2018, **1**, 6227–6233.
50 M. Neophytou, M. De Bastiani, N. Gasparini, E. Aydin, E. Ugur, A. Seitkhan, F. Moruzzi, Y. Choaie, A. J. Ramadan, J. R. Troughton, R. Hallani, A. Savva, L. Tsetseris, S. Inal, D. Baran, F. Laquai, T. D. Anthopoulos, H. J. Snaith, S. De Wolf and I. McCulloch, *ACS Appl. Energy Mater.*, 2019, **2**, 8090–8097.
51 L. Qiu, S. He, L. K. Ono, S. Liu and Y. Qi, *ACS Energy Lett.*, 2019, **4**, 2147–2167.
52 S. K. Hau, Y.-J. Cheng, H.-L. Yip, Y. Zhang, H. Ma and A. K. Y. Jen, *ACS Appl. Mater. Interfaces*, 2010, **2**, 1892–1902.
53 C. Murawski, C. Fuchs, S. Hofmann, K. Leo and M. C. Gather, *Appl. Phys. Lett.*, 2014, **105**, 113303.
54 M. L. Tietze, J. Benduhn, P. Pahner, B. Nell, M. Schwarze, H. Kleemann, M. Krammer, K. Zojer, K. Vandewal and K. Leo, *Nat. Commun.*, 2018, **9**, 1182.
55 P. K. Koech, A. B. Padmaperuma, L. Wang, J. S. Swensen, E. Polikarpov, J. T. Darsell, J. E. Rainbolt and D. J. Gaspar, *Chem. Mater.*, 2010, **22**, 3926–3932.
56 C. Yongyoon, S. A. Mahboubi, Y. J. Sung, K. Jincheol, L. D. Seul, S. Jan, D. Xiaofan, M. A. Green, H. Shujuan and A. W. Y. Ho-Baillie, *Adv. Energy Mater.*, 2018, **8**, 1703392.
57 E. Aydin, M. De Bastiani, X. Yang, M. Sajjad, F. Aljamaan, Y. Smirnov, M. N. Hedhili, W. Liu, T. G. Allen, L. Xu, E. Van Kerschaver, M. Morales-Masis, U. Schwingenschlögl and S. De Wolf, *Adv. Funct. Mater.*, 2019, **0**, 1901741.
58 J. Saska, G. Gonel, Z. I. Bedolla-Valdez, S. D. Aronow, N. E. Shevchenko, A. S. Dudnik, A. J. Moulé and M. Mascal, *Chem. Mater.*, 2019, **31**, 1500–1506.
59 W. K. Metzger, I. L. Repins, M. Romero, P. Dippo, M. Contreras, R. Noufi and D. Levi, *Thin Solid Films*, 2009, **517**, 2360–2364.
60 C. Ding, Y. Zhang, F. Liu, Y. Kitabatake, S. Hayase, T. Toyoda, K. Yoshino, T. Minemoto, K. Katayama and Q. Shen, *Nano Energy*, 2018, **53**, 17–26.
61 T. Minemoto and M. Murata, *Sol. Energy Mater. Sol. Cells*, 2015, **133**, 8–14.
62 Q. Wang, F. Zu, P. Caprioglio, C. M. Wolff, M. Stolterfoht, M. Li, S.-H. Turren-Cruz, N. Koch, D. Neher and A. Abate, *ACS Energy Lett.*, 2020, **5**, 2343–2348.
63 B. Chen, S.-W. Baek, Y. Hou, E. Aydin, M. De Bastiani, B. Scheffel, A. Proppe, Z. Huang, M. Wei, Y.-K. Wang, E.-H. Jung, T. G. Allen, E. Van Kerschaver, F. P. García de Arquer, M. I. Saidaminov, S. Hoogland, S. De Wolf and E. H. Sargent, *Nat. Commun.*, 2020, **11**, 1257.
64 J. M. Richter, M. Abdi-Jalebi, A. Sadhanala, M. Tabachnyk, J. P. H. Rivett, L. M. Pazos-Outón, K. C. Gödel, M. Price, F. Deschler and R. H. Friend, *Nat. Commun.*, 2016, **7**, 13941.
65 W. Tress, *Adv. Energy Mater.*, 2017, 1602358, DOI: 10.1002/aenm.201602358.
66 A. Delamarre, L. Lombez and J.-F. Guillemoles, *J. Photonics Energy*, 2012, **2**, 027004.
67 G. El-Hajje, C. Momblona, L. Gil-Escrig, J. Ávila, T. Guillemot, J.-F. Guillemoles, M. Sessolo, H. J. Bolink and L. Lombez, *Energy Environ. Sci.*, 2016, **9**, 2286–2294.
68 W. Raja, A. Bozzola, P. Zilio, E. Miele, S. Panaro, H. Wang, A. Toma, A. Alabastri, F. De Angelis and R. P. Zaccaria, *Sci. Rep.*, 2016, **6**, 24539.
69 W. Raja, M. Schmid, A. Toma, H. Wang, A. Alabastri and R. P. Zaccaria, *ACS Photonics*, 2017, **4**, 2025–2035.
70 P. Giannozzi, S. Baroni, N. Bonini, M. Calandra, R. Car, C. Cavazzoni, D. Ceresoli, G. L. Chiarotti, M. Cococcioni, I. Dabo, A. Dal Corso, S. de Gironcoli, S. Fabris, G. Fratesi, R. Gebauer, U. Gerstmann, C. Gougoussis, A. Kokalj, M. Lazzeri, L. Martin-Samos, N. Marzari, F. Mauri, R. Mazzarello, S. Paolini, A. Pasquarello, L. Paulatto, C. Sbraccia, S. Scandolo, G. Sclauzero, A. P. Seitsonen, A. Smogunov, P. Umari and R. M. Wentzcovitch, *J. Phys.: Condens. Matter*, 2009, **21**, 395502.
71 J. P. Perdew and Y. Wang, *Phys. Rev. B: Condens. Matter Mater. Phys.*, 1992, **46**, 12947–12954.
72 P. E. Blöchl, *Phys. Rev. B: Condens. Matter Mater. Phys.*, 1994, **50**, 17953–17979.
73 S. Grimme, *J. Comput. Chem.*, 2006, **27**, 1787–1799.
74 H. J. Monkhorst and J. D. Pack, *Phys. Rev. B: Solid State*, 1976, **13**, 5188–5192.
75 K. Momma and F. Izumi, *J. Appl. Crystallogr.*, 2011, **44**, 1272–1276.

 This journal is © The Royal Society of Chemistry 2021